Three-dimensional effects of curved plasma actuators in quiescent air

Chin-Cheng Wang, Ryan Durscher, and Subrata Roy[a)]
Computational Plasma Dynamics Laboratory and Test Facility, Applied Physics Research Group, Department of Mechanical and Aerospace Engineering, University of Florida, Gainesville, Florida 32611, USA

(Received 23 January 2011; accepted 19 March 2011; published online 29 April 2011)

This paper presents results on a new class of curved plasma actuators for the inducement of three-dimensional vortical structures. The nature of the fluid flow inducement on a flat plate, in quiescent conditions, due to four different shapes of dielectric barrier discharge (DBD) plasma actuators is numerically investigated. The three-dimensional plasma kinetic equations are solved using our in-house, finite element based, multiscale ionized gas (MIG) flow code. Numerical results show electron temperature and three dimensional plasma force vectors for four shapes, which include linear, triangular, serpentine, and square actuators. Three-dimensional effects such as pinching and spreading the neighboring fluid are observed for serpentine and square actuators. The mechanisms of vorticity generation for DBD actuators are discussed. Also the influence of geometric wavelength (λ) and amplitude (Λ) of the serpentine and square actuators on vectored thrust inducement is predicted. This results in these actuators producing significantly better flow mixing downstream as compared to the standard linear actuator. Increasing the wavelengths of serpentine and square actuators in the spanwise direction is shown to enhance the pinching effect giving a much higher vertical velocity. On the contrary, changing the amplitude of the curved actuator varies the streamwise velocity significantly influencing the near wall jet. Experimental data for a serpentine actuator are also reported for validation purpose. © *2011 American Institute of Physics*. [doi:10.1063/1.3580332]

I. INTRODUCTION

The plasma actuator is becoming a popular device for active flow control. A few advantages of the plasma actuators are surface compliance, rapid response, lack of moving parts, and easy installation. Specifically, due to the lack of mechanical components, the lifetime of the actuator could be significantly extended as compared to other mechanical/electromechanical devices such as synthetic jet actuators. Reported experimental and numerical results[1,2] show that dielectric barrier discharge (DBD) actuators are effective in controlling the flow at low freestream velocities (~20 m/s). One major impediment affecting the working speed of an actuator is the inducement of a thin boundary layer that is limited by wall shear. It may be possible to increase the effectiveness of the plasma actuator by designing a specific actuator[3] that can penetrate deeper into the freestream boundary layer. Figure 1 shows a 10-fold increase in the boundary layer thickness due to the plasma pinching effect. The pinching effect is induced by a single decomposed half-wave, which is also called a plasma horseshoe actuator. In this paper, we will study the serpentine actuator both numerically and experimentally. The serpentine configuration consists of a set of horseshoe actuators connected side by side.

Many researchers[4,5] have demonstrated aerodynamic applications of standard DBD actuators on a flat plate at atmospheric pressure. These actuators produced reasonable thrust by asymmetric spanwise electrode configurations. Numerical models of such configurations range from simplified estimations of the force field with an assumed plasma distribution to detailed air chemistry based plasma kinetic simulations.[6–9] Other researchers have developed reduced order force models[8] based on semiempirical[6,7] or physics based formulations.[9] In these reduced order models, not only the actuator geometry but also the electrical parameters were taken into account. The fidelity of these methods is better than that of the phenomenological models but has yet to explain the operational physics of DBD actuators. Also, the same reduced order models that may work well for a standard linear actuator may fall short for the serpentine configuration due to a lack of physical understanding. First-principles analysis of a plasma actuator provides for a high-fidelity numerical framework by which the physics of the problem may be examined. While it is feasible to incorporate a large number of species into the air chemistry model, it becomes computationally impractical to solve them for a DBD actuator operated in the kilohertz frequency regime. A reasonable way around this problem is to solve a coupled system of plasma governing equations for relevant charged (and, if necessary, neutral) species along with Poisson's equation. This is generally referred to as the physics based first-principles analysis. Roy *et al.*[10–12] presented a well-established drift-diffusion model to describe temporal and spatial profiles of voltage distribution, and densities of electrons, positive and negative charged and neutral species. They demonstrated the model predictions for charge densities, electric field, and gas velocity distributions and showed trends that mimic reported experimental data.

Experiments and numerical simulations have repeatedly shown that low speed flows are significantly influenced by plasma actuation.[13,14] Two assumptions are generally made when numerically modeling a DBD actuator in a freestream

[a)]Electronic mail: roy@ufl.edu.

flow: (1) the effect of the plasma manifests itself as a local body force on the working fluid and (2) the body force is primarily two dimensional with negligible crosswise variation. For example, Gaitonde *et al.*[13] and Visbal *et al.*[14] numerically investigated stall mitigation on a NACA0015 airfoil for a reference Reynolds number of up to 90,000. In their studies, the three-dimensional vortical structures were analyzed using essentially two-dimensional plasma effects. Such results give insight to the flow response. However, two-dimensional plasma characterization severely limits the full exploration of the actuator design and its capability.

Examples of three-dimensional plasma actuators are the serpentine and horseshoe shaped configurations.[3] These designs have been shown to have a three-dimensional nature to the plasma force, which induces a mixing type flow. In our prior study,[3] we presented the interaction of a serpentine actuator with a co-flow or counter-flow on a flat surface. We used physics based reduced order models[8] to approximate the plasma forces and incorporated them into Navier–Stokes equations as body forces. The results showed three-dimensional plasma effects extract momentum from an upstream flow injecting it into the bulk fluid through localized pinching and spreading effects. Such three-dimensional actuators produced better flow mixing downstream of the actuator than the standard two-dimensional (linear) DBD actuators.

In the present study, we introduce triangular and square actuators and compare them with the linear and serpentine actuators. For high-fidelity force distribution of these designs, we employ physics based first-principles analysis to resolve the plasma force vectors distribution over a flat surface. Furthermore, we identify the effects of the geometric wavelength and amplitude of the serpentine and square actuators. The details of the numerical model are summarized in Sec. II. Section III describes the numerical problem description and experimental setup of the different plasma actuators investigated. The results showing plasma force vectors, electron temperature, and flow characteristics including velocity distribution and vorticity generation are discussed in Sec. IV. Finally, conclusions and future works are drawn in Sec. V.

II. MODEL DETAILS

The three-dimensional drift-diffusion plasma governing equations as well as Navier–Stokes equations are solved in this study. We utilize the two-species basic model to reduce the computational complexity of plasma chemistry in three dimensions. The unsteady transport for ions and electrons is derived from the first principles in the form of conservation of species continuity. The three-dimensional equations for determining concentrations of positive ions n_i and electrons n_e together with Poisson equation for electric field vector $\mathbf{E}$ (:E_x, E_y, E_z) are described in prior publication.[15] The discharge is maintained using a Townsend ionization scheme. The charged species β (: e,i) is given by the drift-diffusion approximation as $n_\beta \mathbf{V}_\beta = \mathrm{sgn}(e)\, n_\beta \mu_\beta \mathbf{E} - D_\beta \nabla n_\beta$. Finally, we end up with the following equations:

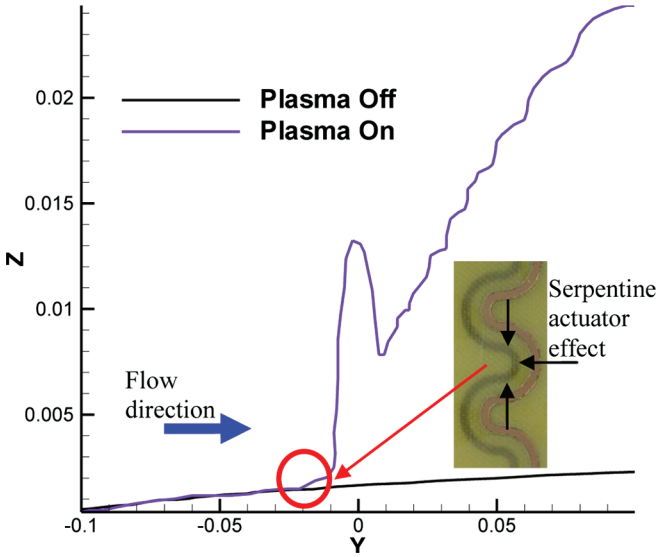

FIG. 1. (Color online) An increase in boundary layer thickness induced by DBD serpentine plasma actuator.

$$\frac{\partial n_\beta}{\partial t} + \frac{\partial}{\partial x}\left\{\mathrm{sgn}(e) n_\beta \mu_\beta E_x - D_\beta \frac{\partial n_\beta}{\partial x}\right\} + \frac{\partial}{\partial y}\left\{\mathrm{sgn}(e) n_\beta \mu_\beta E_y - D_\beta \frac{\partial n_\beta}{\partial y}\right\} + \frac{\partial}{\partial z}\left\{\mathrm{sgn}(e) n_\beta \mu_\beta E_z - D_\beta \frac{\partial n_\beta}{\partial z}\right\} = \alpha|\Gamma_e| - r n_i n_e. \quad (1)$$

where $\mu_i = 1.45 \times 10^3/\mathrm{p}$ ($\mathrm{cm}^2/\mathrm{sV}$) is the ion mobility, $\mu_e = 4.4 \times 10^5/\mathrm{p}$ ($\mathrm{cm}^2/\mathrm{sV}$) is the electron mobility, D_i and D_e are the ion and electron diffusion coefficients calculated from the Einstein relation, which is a function of ion and electron mobility as well as ion and electron temperature, that is, $D_i = \mu_i T_i$ and $D_e = \mu_e T_e$.

We assume that the electrons are in local thermal equilibrium (LTE), and the mean energy of the streamer head equilibrates in the presence of the electric field as a function of local (E/N). The electron temperature T_e in the plasma is proportional to the ratio of the electric field to the density of neutral particles (E/N). The electron temperature in electron volts can be determined according to the expression, $T_e = (E/N)/(2\sigma\sqrt{2m_e/m_i})$, where σ is the cross-section of electron–neutral collisions.[16] We consider isothermal ions and neutrals.

A domain of $(-0.0396{:}0.0396 \times -0.0216{:}0.0216 \times 0.0{:}0.024)$ m is considered for the plasma simulation. A 2.4 mm thick Teflon dielectric is used with a relative dielectric constant of 2. The mesh consists of $89 \times 49 \times 41$ nodes. The numerical model for solving DBD plasma governing equations uses an efficient finite element algorithm for solving partial differential equations (PDE) approximately. The solution methodology anchored in the in-house modular MIG flow code is based on the Galerkin weak statement (GWS) of the PDE that is derived from variational principles. An iterative sparse matrix solver, generalized minimal residual (GMRES), is utilized to solve the resultant stiff matrix. The fully implicit time stepping procedure along with the

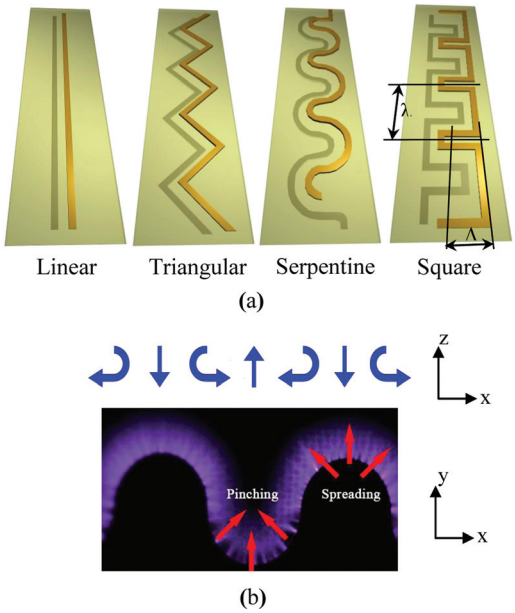

FIG. 2. (Color online) (a) Schematics of shaped plasma actuators for linear, triangular, serpentine, and square designs. (b) A clear illustration of three-dimensional effects of pinching and spreading for serpentine plasma actuator.

Newton–Raphson scheme is used for dealing with this nonlinear problem. The solution is assumed to have converged when the L_2 norms of all the normalized solution variables and residuals are below a convergence criterion of 10^{-3}.

The time average of the spatial distribution of electric force density, $\mathbf{F}$ $(:F_x, F_y, F_z) = eq\mathbf{E}$, is introduced into the commercial Navier–Stokes solver, ANSYS FLUENT, as a source term in the momentum equations using user defined functions (UDF). A second-order upwind spatial discretization method is used to solve for the induced flow on a computational mesh of 500,000 fluid volumes. Convergence is determined when the residual among the continuity and momentum equations are less than 10^{-3}.

III. PROBLEM DESCRIPTIONS

A. Computation

Figure 2(a) depicts a schematic of standard linear, triangular, serpentine, and square plasma actuators. The actuators consist of powered and grounded electrodes separated by a dielectric material. The plasma actuators are assumed to be flushed mounted at the center of a quiescent domain with dimensions $(-0.1{:}0.1 \times -0.1{:}0.1 \times 0{:}0.1)$ m. The right side of the domain ($y = 0.1$ m) is considered to be the inlet, while the top ($z = 0.1$ m) and left ($y = -0.1$ m) sides are outflow boundaries. The gauge pressure at the outlet boundaries is maintained at 0 Pa. Symmetry is considered on the domain's side walls ($x = \pm 0.1$ m), while no slip is enforced on the lower boundary ($z = 0.0$ m). The thickness of the dielectric material and electrodes are neglected in the flow simulations. Air is considered to be the working fluid.

The three-dimensional effects of plasma actuators are studied based on the four different shapes seen in Fig. 2(a). Upon applying a sufficient electric field to the exposed electrode to induce an electrical breakdown, an electrohydrodynamic (EHD) body force is generated along to electrode [Fig. 2(b)]. This electric force interacts with bulk fluid and induces vortices locally and downstream of the actuator. Figure 2(b) shows the serpentine actuators pinching and spreading effects on the fluid in the xy-plane. Such effects induce a three-dimensional swirling flow in the vicinity of the plasma region. The mechanisms of vorticity generation using the serpentine actuator will be explained in Sect. IV.

The second part of this paper is to investigate serpentine and square actuators with three different wavelengths (λ) and amplitudes (Λ) shown in the Fig. 2(a). For the cases of changing wavelengths, the wavelength is varied from 10 to 30 mm with the amplitude fixed at 8 mm. On the other hand, the amplitude is increased from 4 to 16 mm for a fixed wavelength of 10 mm.

B. Actuator construction and experiment setup

A photo-fabrication method is used to construct the continuously curved electrode shape of the serpentine actuator. Copper tape was first adhered to both sides of a 3 mm thick acrylic plate. A negative photo-resist, a transparent film, and a UV light were then employed to imprint the specific serpentine design on the copper, which was then selectively removed after being submerged in a bath of ferric chloride. The width of the exposed and grounded electrode is 2 mm, which is kept at a uniform horizontal gap of 2 mm. The serpentine actuator used is constructed from patterned circular arcs. The wavelength (λ) of this design is 20 mm, and the amplitude (Λ) is 8 mm. To prevent end effects from influencing the velocity measurements, the tested actuators consisted of 4.5 periods for an overall crosswise length of 90 mm.

The nonintrusive optical diagnostic technique of particle image velocimetry (PIV) is used to visualize and measure the induce flow field. The actuator is setup in a $61 \times 61 \times 120$ cm

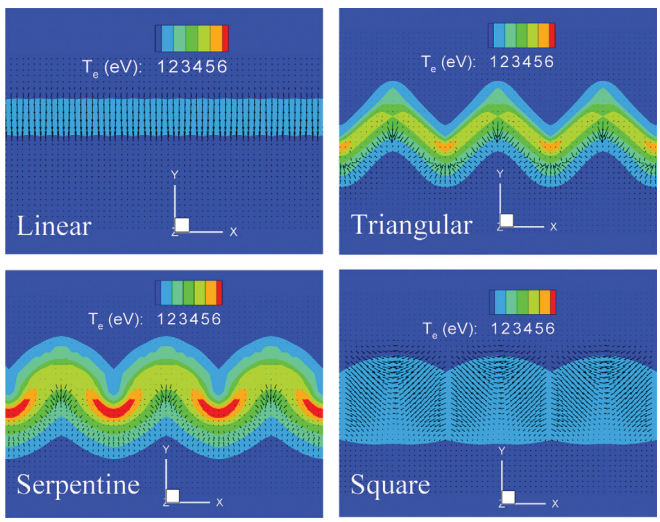

FIG. 3. (Color online) Electron temperature contour on the xy plane for linear, triangular, serpentine, and square actuators.

quiescent chamber, which is seeded with vaporized Ondina oil. A light sheet cutting along the span of the actuator was generated using a Nd:YAG, dual cavity pulsed, 532 nm laser (New Wave Research Solo PIV II 30). A *LaVision*'s Imager Intense (1376×1040 pixels) camera was used to capture the PIV images. The field of view for each image was approximately 40×30 mm. The floor of the chamber is connected to a translational traverse (Velmex A1503P40-S1.5) allowing it to move ± 19 mm off center. This allows the measurement plane along the span of the actuator to be easily selected without having to readjust the light sheet each time.

IV. RESULTS AND DISCUSSIONS

A. Changing shapes

The four different actuator configurations [Fig. 2(a)] are simulated in quiescent air. We assume a time averaged plasma force as a body source term in the flow domain. The intensity of the plasma force is based on the electric field and charge separation. One way to examine the variation of the plasma force distribution is to measure electron temperature (Fig. 3). For a weakly ionized gas, the electron temperature ($\sim$eV) can be two orders of magnitude higher than the ions or neutral species. Basically, the electron temperature is proportional to the ratio E/N (electric field/neutral density). Figure 3 shows the electron temperature distribution for four different plasma actuators. The results predict that the electron temperatures increase for triangular, serpentine, and square actuators due to the geometric effects.

Figure 4(a) shows force vectors overlaid on potential contours in the xy plane ($z = 0$) for linear, triangular, serpentine, and square actuators. In the figure, the force vectors are acting from the powered electrode (red) to the grounded electrode (blue) for each shape. From the top view of the linear actuator, the force vectors are even and perpendicular to the electrodes. For the serpentine actuator, the force vectors follow the shape of semicircle electrode. Also, the electric force vectors for triangular and serpentine actuators are much larger than the linear case. This is a result of the concentrated electric fields as a result of the electrode geometry. Based on these results, it is clear that the shape of the electrode has a significant influence on the magnitude and distribution of the plasma body force. Figure 4(b) shows electric force vectors overlaid on force (F_y) contours in the yz plane ($x = 0$) at center of the actuator. The force resulting from the linear configuration is predominately parallel to the surface, while the other actuators produce a force that follows more of a projectile profile that stems from the powered electrode to the grounded electrode. From Fig. 4, it is clear to see the force distributions are purely three dimensional for the triangular, serpentine, and square designs.

Figure 5 shows the stream traces overlaid on vertical velocity contours (z velocity) for the yz plane ($x = 0$). We can see the flow is attracted from the inlet (right) and is pinched at center ($y = 0$) of the domain and then moves forward downstream of the actuators. The streamtraces also show that the flow is moving upward downstream after the pinching region. For the linear actuator, there is no pinching

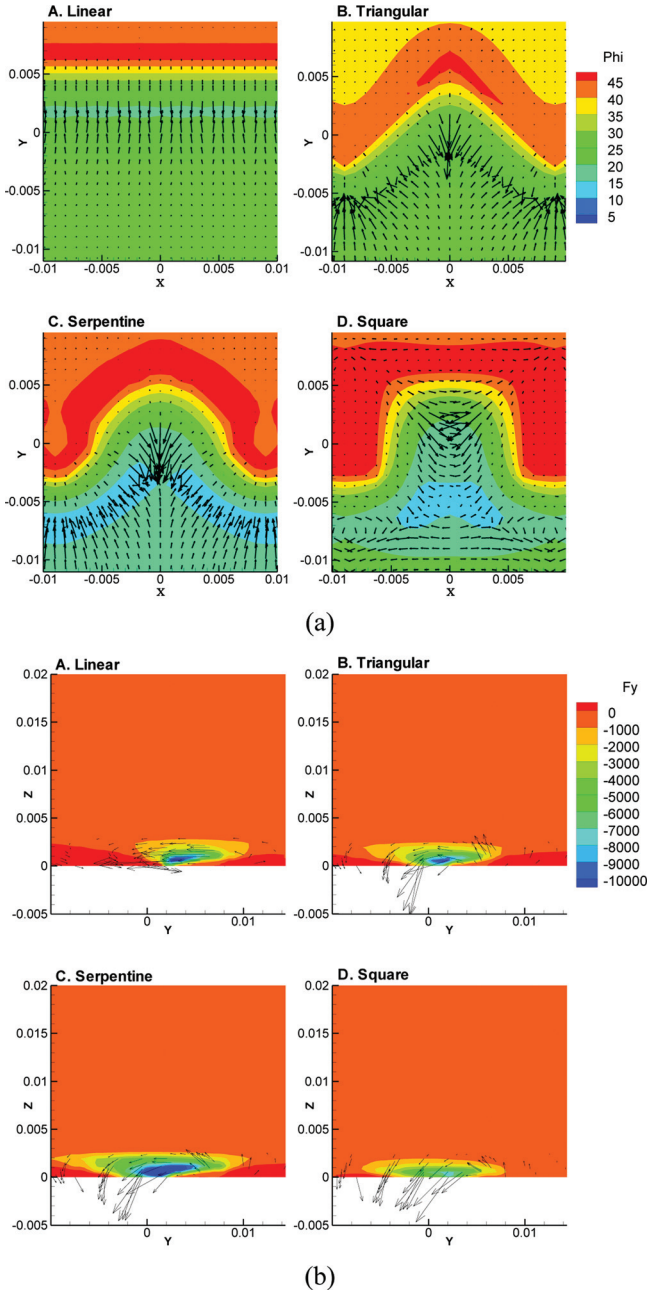

FIG. 4. (Color online) Plasma force vectors overlaid on (a) potential contour (Phi) at the xy plane and (b) force contour (Fy) in y direction at the yz plane for four different designs.

effect, so the plasma induced surface jet is issued in an approximate angle of 8°. For the triangular actuator, there is a little pinching effect with the resulting jet angle being approximately 12°. This is only slightly higher than the linear actuator. For the serpentine and square designs, the pinching effects result in a large normal velocity away from the wall. Here the numerically predicted jet issuing angle is approximately 23 and 33 degrees for the serpentine and square actuators, respectively. Based on jet angles of the plasma actuators, we can say that the serpentine and square actuators have much stronger three-dimensional (pinching) effects than the two-dimensional linear actuator.

Figure 6 shows instantaneous three-dimensional *vortical* structures that are induced by the four different actuators

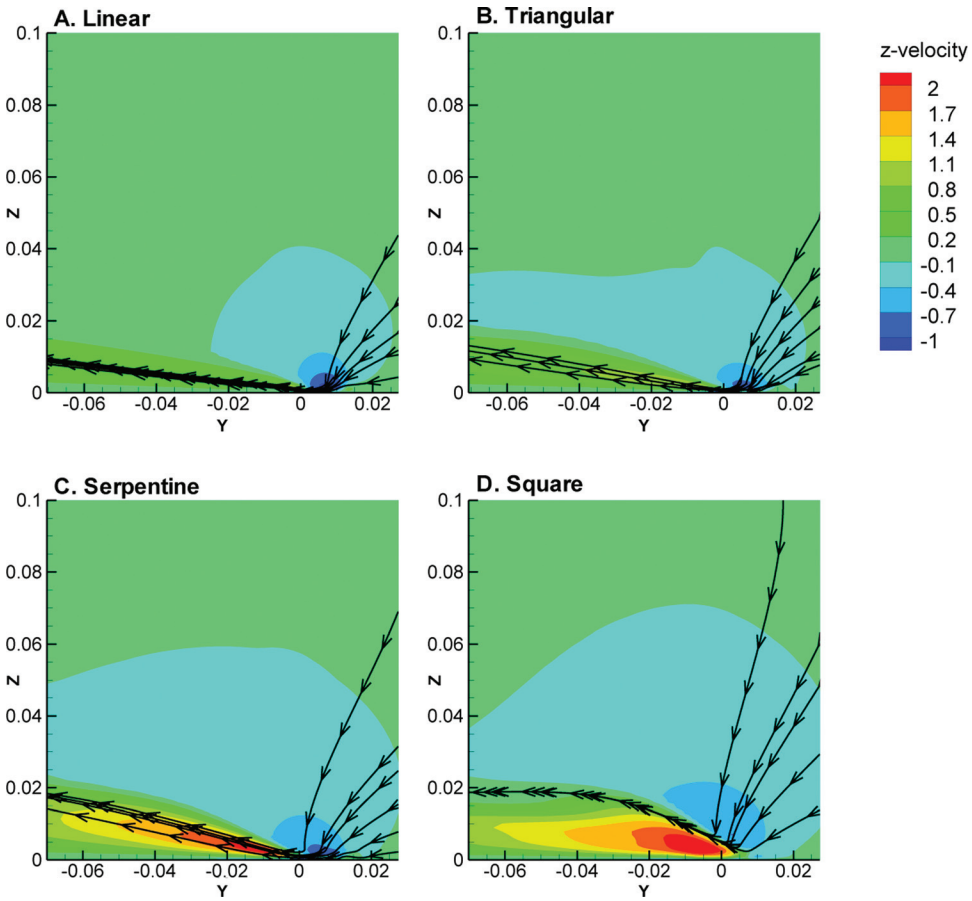

FIG. 5. (Color online) Streamtraces overlaid on vertical velocity contour (z velocity) at the yz plane for four different designs.

after 16 ms of operation. In Fig. 6, the iso-surfaces colored by red and blue depict y vorticity (ω_y, that is, streamwise vorticity) levels at $\pm$ 1000 1/s. For the two-dimensional linear actuator (baseline case), the flow is primarily in the streamwise (y) direction [with a small vertical (z) component]. Thus the standard linear actuator produces very little streamwise (y) and normal (z) vorticity downstream of the actuator. For the three-dimensional (triangular, serpentine, and square) actuators, the fluid is pushed in all three directions, which increases vorticity generation. Specially, the streamwise y vorticity dominates the flow field of the serpentine and square actuators. This represents the rapid changes in spanwise velocity, which causes the pinching and spreading effects. The pinching effect changes the flow direction from surface normal to surface parallel, while the spreading effect pushes the fluid outward and away from the actuator. When both effects act at same the time, they result in rapid rotational and translational motions of the fluid in all three directions. Notably, serpentine and square actuators are capable of inducing mixing much further downstream (in the y direction) than the baseline two-dimensional linear actuator. The square actuator, in particular, generates strong vortical structures further downstream than the other designs. Such a design could be a very useful solid state device for increasing the local mixing of a surrounding fluid. A detailed look at the of vorticity generation resulting from a square actuator is presented in Fig. 7. The figure depicts counter-rotating vortex pairs, which propagate downstream. In the pinching regions, we can see the counter-rotating vortex pairs grow as they propagate downstream. On the contrary, the flow attaches on the flat surface in the spreading regions. Due to end effects, a stronger vorticity is generated near the spanwise edges of the electrodes for all the actuators.

B. Changing wavelengths and amplitudes

From the previous discussion, we observed that the serpentine and square actuators have a much stronger three-dimensional vortical effect on the flow than the other two designs. The computed representative velocity distributions are presented here. Figure 8 (top) plots a serpentine design with a longer wavelength (30 mm) but shorter amplitude (4 mm). The force vectors follow the curved shape of the electrodes. Velocity contour lines of u, w, v are plotted on along the xy plane ($z = 0.001$ m). In the pinching regions, spanwise velocity (u) is varied from -1 to 1 m/s with symmetry. A vertical velocity (w) of 0.5 m/s and a streamwise velocity (v) of -6 m/s also exist in this region, which indicates that the flow is moving upward and forward. Based on preceding results, we can understand three-dimensional flow behaviors induced by these plasma electric force vectors. Subsequently, we focus on five different cases for both serpentine (left column) and square actuator (right column) shown in Fig. 9. The figure depicts streamtraces overlaid on the vertical velocity contour (z velocity) cut along the yz plane. The influence of different wavelengths ($\lambda = 10$, 20, 30 mm) or

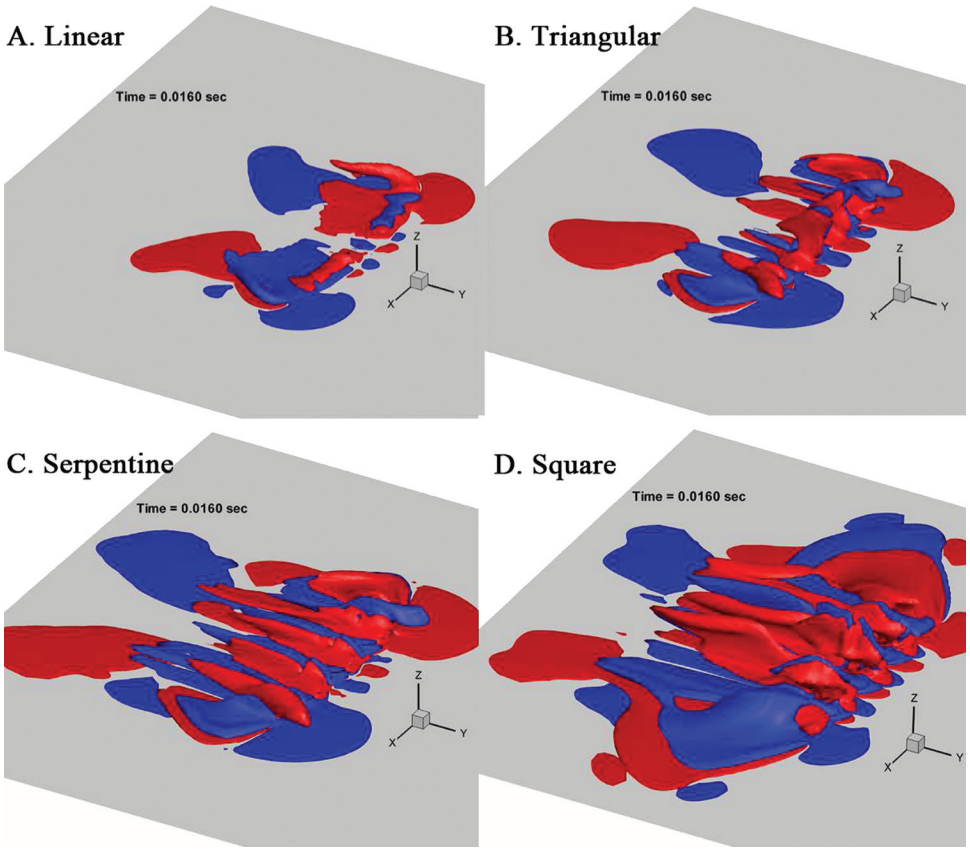

FIG. 6. (Color online) Three-dimensional dynamics of *y* vorticities of +1000 1/s (red) and −1000 1/s (blue) at 16 ms for four different designs.

amplitudes ($\Lambda = 4$, 8, 16 mm) is presented. It is obvious to see that the vertical velocity of the flow increases as the wavelengths increases from $\lambda = 10$ to $\lambda = 20$ mm for both designs. On the contrary, for a fixed wavelength (10 mm), varying the amplitude has little effect of the resultant vertical velocity for either design. The large increase in vertical velocity for the square configuration as compared to the serpentine actuator is attributed to the larger ionized area/region produced by the square design [Fig. 2(a)]. From the streamtraces in Fig. 9, the near wall jet angle changes significantly as the actuators wavelength increases. In particular the jet angle increases almost 100% as the wavelength of the square actuator increases from 10 to 20 mm. However, the jet angle does not increase linearly with a further increase in wavelength. As the jet angle increases, the vertical component of the flow velocity increases. In other words, the decreasing jet

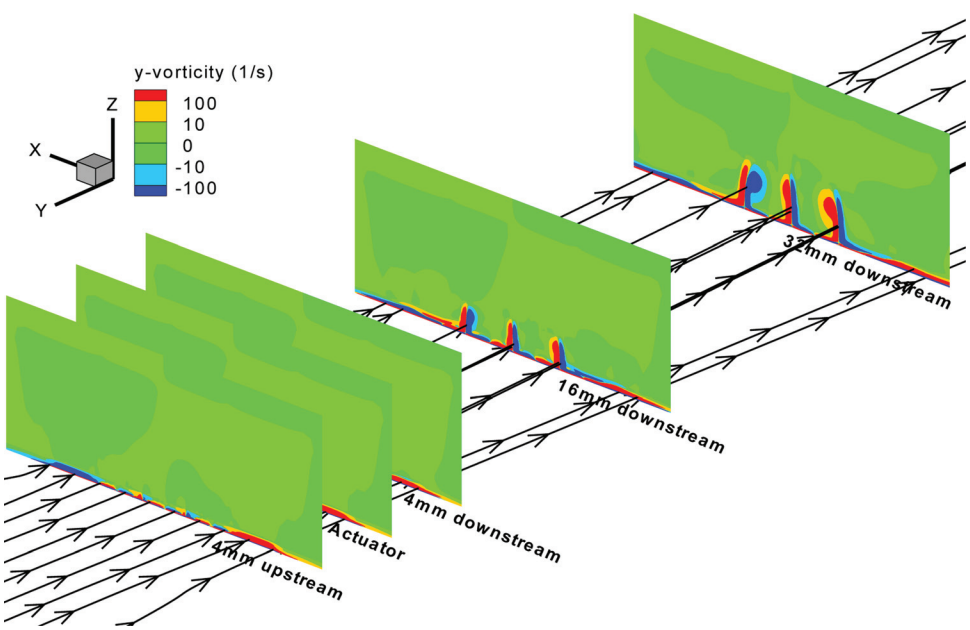

FIG. 7. (Color online) Velocity streamtraces and vorticity contours (*y* vorticity) in streamwise direction at five different spanwise planes (*xz* plane) for the square actuator.

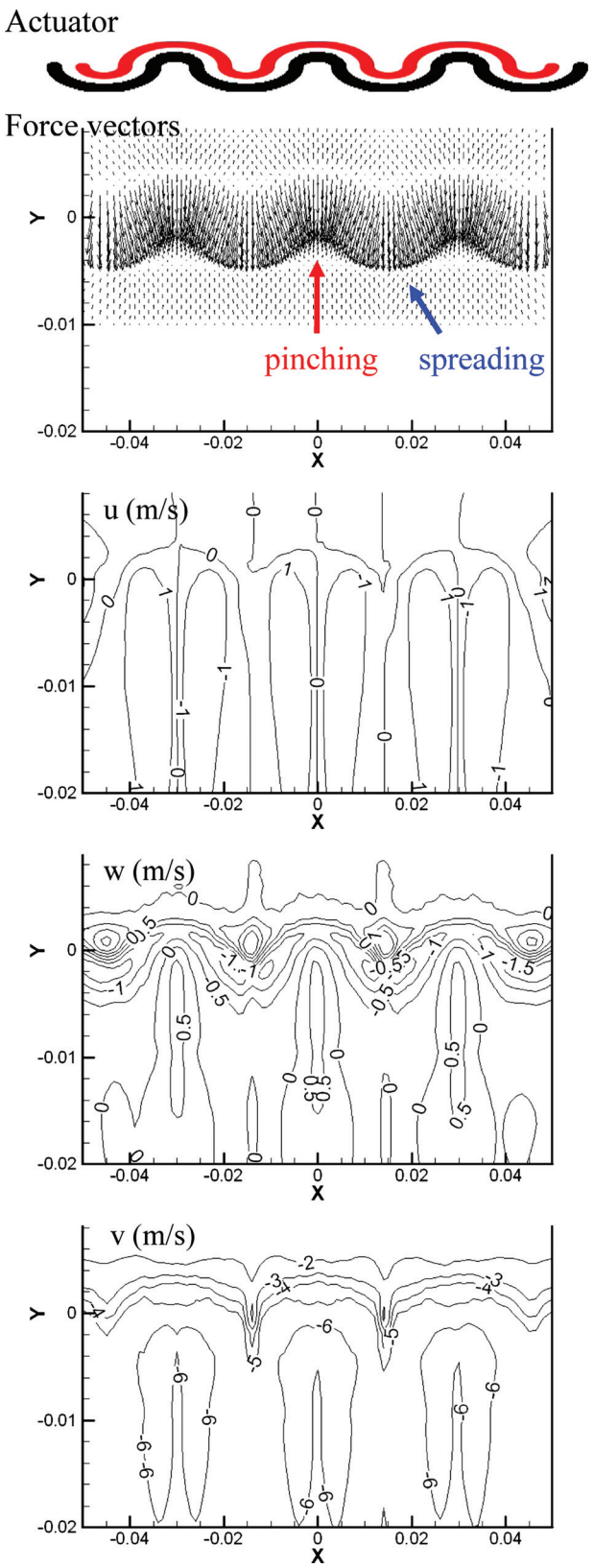

FIG. 8. (Color online) Plasma force vectors of serpentine actuator induced fluid flow in three dimensions on the *xy* plane.

angle means the streamwise velocity becomes dominant. Based on these results, we conclude that different flow physics may be triggered by manipulation of the actuators wavelength and amplitude. Depending on the particular application of the plasma actuator, different effects may be more beneficial than others.

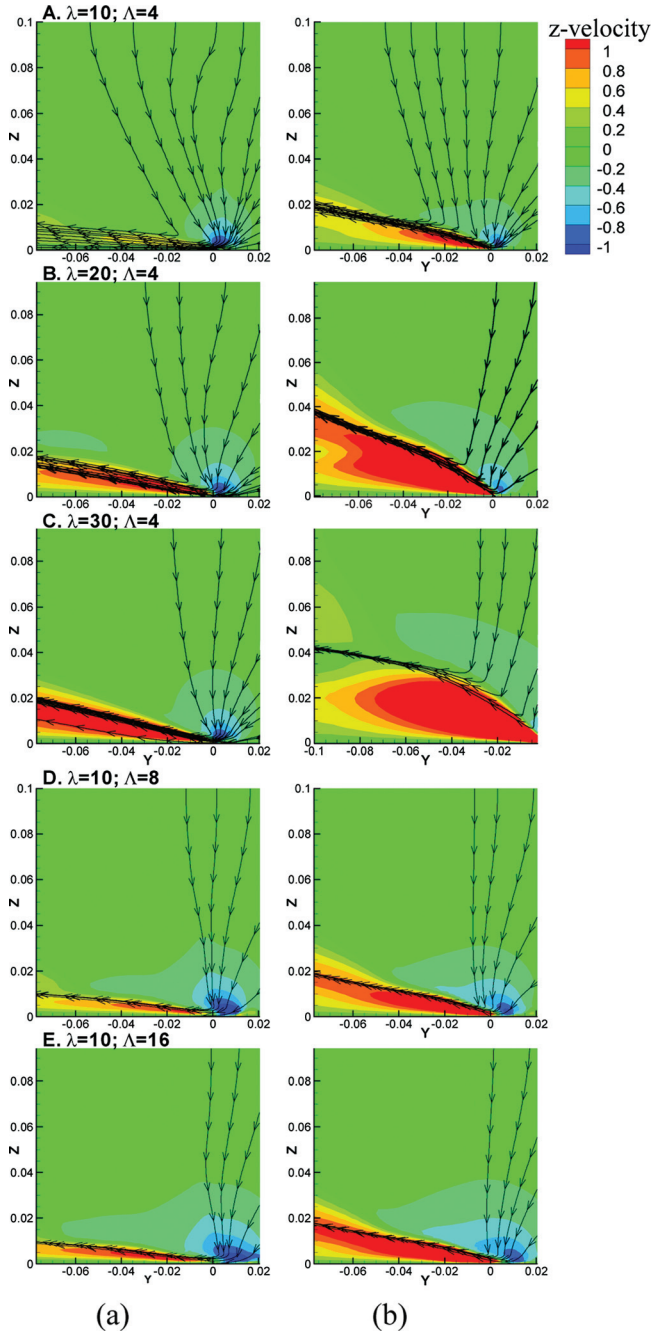

FIG. 9. (Color online) *z*-velocity contour distribution with variables of wavelengths and amplitudes on *yz* plane for (a) serpentine and (b) square actuators.

C. Experimental data for a serpentine actuator

The induced flow field was measured along the span of the actuator with a planar PIV system as described in the preceding text. The measurements elucidate the complicated flow physics induced by the serpentine actuator. Figure 10 depicts the velocity magnitude of the time averaged vector field overlaid with streamtraces for five different vertical planes ($x = 0$, 2.5, 5.0, 7.5, and 10.0 mm), along the span of the actuator. The pinching and spreading effects are clearly

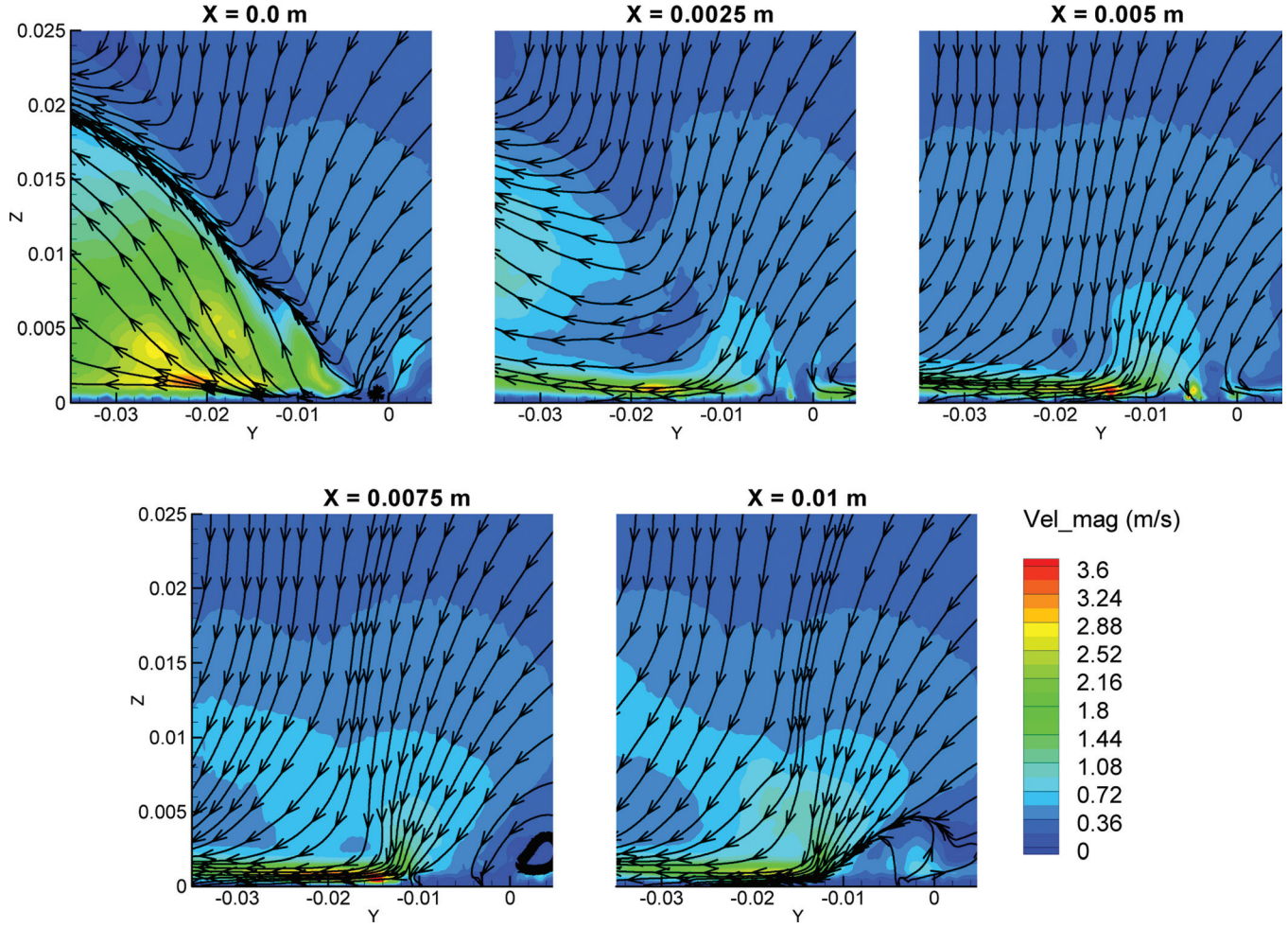

FIG. 10. (Color online) Velocity magnitude of the time averaged vector field overlaid with streamtraces for five vertical planes (*yz* plane) along the span of the serpentine actuator (18.5 kVpp input).

visible at the trough ($x = 0$) and crest ($x = 10$ mm) locations, respectively. Specifically at the trough, the directed jet shows a maximum inducement angle of ~35°. Figure 11 represents the vertical velocity contours for a serpentine actuator that closely validates the numerical prediction with experimental data.

Figure 12 shows the results of the jet angles for serpentine and square actuators with different wavelengths and amplitudes. For cases of the fixed wavelength of 10 mm, the serpentine and square actuators show a similar tendency as the amplitudes increase. The jet angle of the square actuator is around three times higher than serpentine actuator. On the other hand, for the cases in which the amplitude is fixed (4 mm) and the wavelength is increased, the jet angle increases for both configurations. In simulation, we numerically predict the highest jet angle is ~36° for the square actuator with wavelength of 20 mm and amplitude of 4 mm. Experimentally a jet angle of ~35° was observed for a serpentine

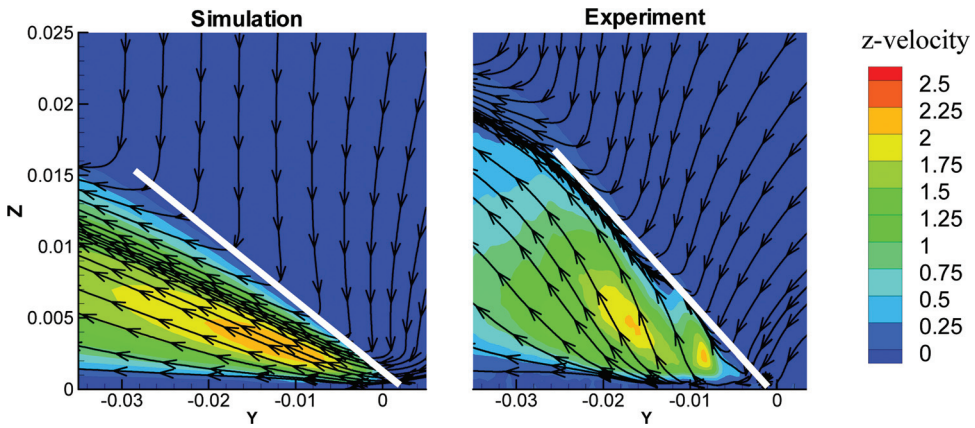

FIG. 11. (Color online) Vertical velocity contour validation with experimental data for a square actuator.

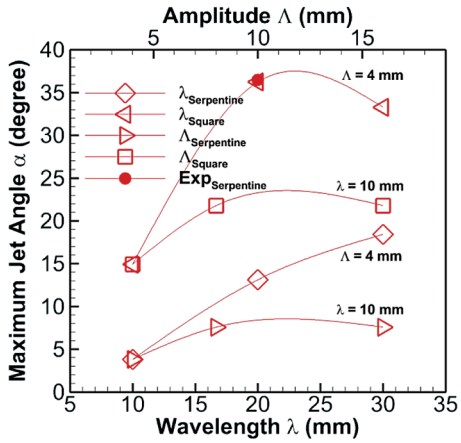

FIG. 12. (Color online) Comparison of numerical and experimental results for the jet angles induced by serpentine and square actuators with different wavelengths and amplitudes.

actuator ($\lambda = 20$ mm and $\Lambda = 8$ mm). The relative agreement between the numerical and experimental findings provides some confidence that the numerical model is capable of predicting reasonable flow characteristics resulting from DBD actuation.

V. CONCLUSIONS

The plasma governing equations as well as Navier–Stokes equations were solved with our in-house MIG flow code and commercial software. The configuration of four different electrodes shapes are introduced in the present study. The results indicate that the linear actuator (or standard actuator) is less effective at introducing streamwise vortical structures as compared to the other design investigated. It was numerically predicted that the serpentine and square designs are capable of producing significant three-dimensional effects; this leads to enhanced mixing of the surrounding fluid. Electron temperature distribution is also shown based on the concentration of electric field for all the designs. The effect of the actuators amplitude and wavelength was also investigated for the serpentine and square configurations. It was found that the induced vertical velocity in the vicinity of the plasma region is proportional to the actuators wavelengths. A maximum jet angle at the trough of the square actuator was numerically predicted to be $\sim 36^\circ$. Experimental data help validate this predication with a measured jet angle of $\sim 35^\circ$ for a serpentine actuator. To more accurately predict the EHD body force, our current plasma numerical modeling may be improved by adding air chemistry and nonequilibrium physics due to the disparate temperature in weakly ionized gas.

[1]E. Moreau, J. Phys. D **40**, 605 (2007).
[2]T. C. Corke, C. L. Enloe, and S. P. Wilkinson, Annu. Rev. Fluid Mech. **42**, 505 (2010).
[3]S. Roy and C.-C. Wang, J. Phys. D **42**, 032004 (2009).
[4]J. R. Roth, D. M. Sherman, and S. P. Wilkinson, "Boundary layer flow control with a one atmosphere uniform glow discharge surface plasma," AIAA Paper No. 98-0328, 1998.
[5]T. C. Corke, E. J. Jumper, M. L. Post, D. M. Orlov, and T. E. McLaughlin, "Application of weakly-ionized plasmas as wing flow-control devices," AIAA Paper No. 2002-350, 2005.
[6]W. Shyy, B. Jayaraman, and A. Andersson, J. Appl. Phys. **92**, 6434 (2002).
[7]D. M. Orlov and T. C. Corke, "Numerical simulation of aerodynamic plasma actuator effects" AIAA Paper No. 2005-1083, 2005.
[8]K. P. Singh and S. Roy, J. Appl. Phys. **103**, 013305 (2008).
[9]K. P. Singh and S. Roy, J. Appl. Phys. **101**, 123308 (2007).
[10]S. Roy, Appl. Phys. Lett. **86**, 101502 (2005).
[11]H. Kumar and S. Roy, Phys. Plasmas **12**, 093508 (2005).
[12]K. P. Singh, S. Roy, and D. V. Gaintonde, "Modeling of dielectric barrier discharge plasma actuator with atmospheric air chemistry," AIAA Paper No. 2006-3381, 2006.
[13]D. V. Gaintonde, M. R. Visbal, and S. Roy, ASME Joint U.S.-European Fluids Engineering Meeting, Miami, FL, 2006, FEDSM2006-98553.
[14]M. R. Visbal and D. V. Gaintonde, AIAA Paper No. 2006-505, 2006.
[15]C.-C. Wang and S. Roy, J. Phys. D **42**, 185206 (2009).
[16]G. A. Galechyan, Laser Phys. **5**, 731 (1995).